

Local Hydrodynamic Stability of Accretion Disks

John F. Hawley, Steven A. Balbus, Wayne F. Winters
 Department of Astronomy, University of Virginia,
 Charlottesville, VA 22903; jh8h, sb, ww5m@virginia.edu

ABSTRACT

We employ a variety of numerical simulations in the local shearing box system to investigate in greater depth the local hydrodynamic stability of Keplerian differential rotation. In particular we explore the relationship of Keplerian shear to the nonlinear instabilities known to exist in simple Cartesian shear. The Coriolis force is the source of linear stabilization in differential rotation. We exploit the formal equivalence of constant angular momentum flows and simple Cartesian shear to examine the transition from stability to nonlinear instability. The manifestation of nonlinear instability in shear flows is known to be sensitive to initial perturbation and to the amount of viscosity; marginally (linearly) stable differentially rotating flows exhibit this same sensitivity. Keplerian systems, however, are completely stable; the strength of the stabilizing Coriolis force easily overwhelms any destabilizing nonlinear effects. In fact, nonlinear effects speed the decay of applied turbulence by producing a rapid cascade of energy to high wavenumbers where dissipation occurs. Our conclusions are tested with grid resolution experiments and by comparison with results from a code that employs an alternative numerical algorithm. The properties of hydrodynamic differential rotation are contrasted with magnetohydrodynamic differential rotation. The kinetic stress couples to the vorticity which limits turbulence, while the magnetic stress couples to the shear which promotes turbulence. Thus magnetohydrodynamic turbulence is uniquely capable of acting as a turbulent angular momentum transport mechanism in disks.

Subject headings: accretion, accretion disks - protostellar disks - instabilities - hydrodynamics

1. Introduction.

In the past few years there has been substantial progress in understanding the origin of angular momentum transport in astrophysical accretion disks (see the reviews by Papaloizou & Lin 1995 and Balbus & Hawley 1998). In particular, the nature of transport by magnetohydrodynamic (MHD) turbulence has been greatly clarified. Magnetized disks are linearly unstable to the weak field magnetorotational instability (Balbus & Hawley 1991). However, in regions surrounding the solar nebula and in protostellar disks more generally, temperatures and densities suggest very small ionization fractions, leading to

magnetic decoupling. The presence of turbulence in such a disk is problematic. For this reason, hydrodynamical studies of disk turbulence remain of great interest.

Before the importance of magnetic fields in disk dynamics was clear, disk turbulence was viewed as a hydrodynamical problem. Adverse entropy gradients (vertical stratification) and adverse angular momentum gradients (radial stratification) each brought with them a legacy of local instability, turbulence and enhanced transport. Moreover, simple shear layers break down into turbulence via nonlinear processes, even in the absence of rotation, and Couette flow experiments show nonlinear breakdown of some Rayleigh-stable velocity profiles (Coles 1965; Drazin & Reid 1981). Even if details were a bit vague, enhanced turbulent transport via *some* hydrodynamic process seemed more than plausible.

Convective models of disk transport are now two decades old (Cameron 1978, Lin & Papaloizou 1980). But convective turbulence does not, by itself, guarantee outward angular momentum transport (Prinn 1990); indeed, recent investigations suggests the opposite. Ryu & Goodman (1992) analyzed the linear stages of convective instability, and pointed out that it produces inward, not outward transport. Kley, Papaloizou & Lin (1993) found inward transport in an axisymmetric disk convection simulation. Stone & Balbus (1996) conducted a full three-dimensional (3D) numerical simulation of the compressible Euler equations in a local patch of Keplerian disk, found small inward transport, and gave arguments as to why this might be expected. Despite the presence of vigorous convection in these simulations, what little net transport was present was directed radially inwards. The time-averaged amplitude of the stress was very small, some three to four orders of magnitude below typical values produced by MHD turbulence in comparable simulations. Similar results were found by Cabot (1996) in a 3D local Navier-Stokes calculation, when the assumed viscosity was sufficiently small.

Shear instabilities have the virtue that any resulting transport will certainly be directed outwards, since the outwardly decreasing angular velocity gradient would be the source of the turbulence. An even older idea that convection (Crawford & Kraft 1956), high Reynolds number shear turbulence as a source of angular momentum transports predates modern accretion disk theory, and is explicitly invoked in Shakura & Sunyaev (1973). Unfortunately, its validity has never been demonstrated. Unlike convective instability, which occurs when a well-understood linear stability criterion is violated, differentially rotating flows are linearly stable by the Rayleigh criterion. The oft-made conjecture is that, despite this, Keplerian disks are nonlinearly unstable, as evinced by some Rayleigh-stable (but decidedly non-Keplerian) Couette flows.

In principle, the nonlinear stability question of hydrodynamical Keplerian disks could be settled by direct numerical simulation. But nonlinear shear instability is a 3D problem, and the critical Reynolds number for the onset of turbulence was thought to be too high to be attainable with a 3D numerical code. This, however is not so (Balbus, Hawley, & Stone 1996; hereafter BHS). Working with the inviscid Euler equations, BHS evolved numerical models at a variety of resolutions, and for a range of angular momentum distributions. A Rayleigh-unstable model produced rapid growth of the perturbation energy, as expected. Simple Cartesian shear flow also produced unstable growth, due to a nonlinear instability. A constant angular momentum distribution also proved to be nonlinearly unstable: this profile is marginally stable to linear perturbations, and BHS used simple symmetry arguments to show that in its stability properties the system is formally equivalent to (unstable) Cartesian shear flow. Thus, 3D simulations *can* reproduce the onset on nonlinear shearing instabilities where they are known to be present.

BHS found that simple shear and constant angular momentum flows were the *only* (unmagnetized) Rayleigh-stable systems to exhibit any dynamical instability. Keplerian disks simulations, in particular, were completely stable. BHS argued that the crucial difference between Keplerian flow and simple shear is the presence of Coriolis forces. The epicyclic oscillations produced by those forces are strongly stabilizing for both linear *and* nonlinear disturbances. Epicyclic oscillations are not present in shear layers or in constant angular momentum rotation profiles, which were found to be the only nonlinear unstable flows. If the velocity profile of a disk has even the most gentle rise in specific angular momentum with radius, its behavior is qualitatively different from the constant angular momentum (or simple shear) case.

At a minimum, the findings of BHS do not augur well for the existence of hydrodynamic turbulent transport in differentially rotating disks. The unfavorable results of the disk convection simulations, combined with the finding that high Reynolds number shear instabilities are easily simulated (when present), but disappear the moment rotational effects are smoothly introduced, suggests that only MHD turbulence offers a viable basis for Shakura-Sunyaev (1973) α -disk models. If hydrodynamic turbulence is present, it must be driven by some source other than differential rotation, and generally will not transport angular momentum (e.g., Balbus & Hawley 1998).

In this paper we return to the local hydrodynamic simulations and consider the hydrodynamic stability problem from several new perspectives. We extend the body of simulations beyond what was done in BHS with higher resolution, and with algorithms which differ in their diffusive properties. In §2 we briefly review the moment equations developed by BHS; these form the basis for interpreting the results of local numerical simulations. In §3 we review numerical procedures used for the local simulations. In §4 we investigate a number of issues: Is there any significant effect due to numerical resolution on BHS’s conclusions regarding the stability of Keplerian flows? BHS speculated that the boundary between nonlinear stability and instability (e.g., near constant angular momentum distributions) should not be sharp, and we confirm this expectation. Nonlinearly unstable, but Rayleigh-stable, laboratory Couette flows are precisely analogous to flows which find themselves at this boundary. We next consider the decay of the applied turbulence in the Keplerian system, at a number of resolutions, and with two distinct numerical schemes. Finally we compare the Reynolds and Maxwell stresses in a series of MHD simulations, which span a full range of background angular momentum distributions. In §5 we present our conclusions.

2. Hydrodynamic Fluctuations

We begin with a brief review of basic disk equations and the formalism of BHS on the nature of hydrodynamic turbulence in disk flows.

Nonadvective transport in a hydrodynamical accretion disk is determined by the Reynolds stress tensor,

$$T_{R\phi} \equiv \langle \rho u_R u_\phi \rangle \quad (1)$$

where ρ is the mass density, and \mathbf{u} is the noncircular component of the velocity \mathbf{v} , i.e., $\mathbf{v} = R\Omega\hat{\phi} + \mathbf{u}$. The average in equation (1) is spatial: we assume that a volume can be found over which the small scale variations average out, leaving $T_{R\phi}$ a smoothly varying

quantity. The phenomenological α prescription of Shakura & Sunyaev (1973) is $T_{R\phi} = \alpha P$, where P is the dynamical pressure (possibly including radiation).

The stress $T_{R\phi}$ has several roles. First, and most familiar, it is the agent of angular momentum and energy transport. We are particularly interested in the radial dependence of $T_{R\phi}$. Consider the average radial angular momentum flux,

$$\langle R\rho v_\phi u_R \rangle \equiv R^2\Omega\langle \rho u_R \rangle + RT_{R\phi}, \quad (2)$$

and the radial energy flux

$$\left\langle \frac{1}{2}\rho v_\phi^2 u_R + \Phi_c \right\rangle = -\frac{1}{2}R^2\Omega^2\langle \rho u_R \rangle + R\Omega T_{R\phi}. \quad (3)$$

where Φ_c is the central (external) gravitational potential. Note that in both equations (2) and (3) the first terms represent advected flux; all nonadvective flux is in the $T_{R\phi}$ contribution of the second terms. Outward transport corresponds to $T_{R\phi} > 0$. The nonadvective contributions differ from one another only by a factor of Ω in the energy flux. Each of the above (net) fluxes is a simple linear combination of $\langle u_R \rangle$ and $T_{R\phi}$ only. The fact that no other flow quantities appear is crucial to the formulation of classical steady-state α disk theories, for it allows for a well-defined luminosity–accretion rate relationship.

The turbulent stress must do more than regulate angular momentum transport, however. It is also the conduit by which free energy is tapped to maintain the fluctuations, which produce $T_{R\phi}$ in the first place. This crucially important role is not a part of standard α disk theory. It is a consequence of *fluctuation* dynamics, not mean flow dynamics. This may be seen by inspecting the diagonal moments of the radial and azimuthal u equations of motion (BHS):

$$\frac{\partial}{\partial t} \left\langle \frac{\rho u_R^2}{2} \right\rangle + \nabla \cdot \left\langle \frac{1}{2} \rho u_R^2 \mathbf{u} \right\rangle = 2\Omega T_{R\phi} - \left\langle u_R \frac{\partial P}{\partial R} \right\rangle - \text{losses} \quad (4)$$

and

$$\frac{\partial}{\partial t} \left\langle \frac{\rho u_\phi^2}{2} \right\rangle + \nabla \cdot \left\langle \frac{1}{2} \rho u_\phi^2 \mathbf{u} \right\rangle = -\frac{\kappa^2}{2\Omega} T_{R\phi} - \left\langle \frac{u_\phi}{R} \frac{\partial P}{\partial \phi} \right\rangle - \text{losses} \quad (5)$$

where “losses” refer to viscous losses. In disks the stress tensor couples both to the Coriolis force and to the background shear, and the former is bigger than the latter.

Contrast this with simple shear flows. Here, only the shear couple is present; the stabilizing Coriolis force is absent. Reverting to Cartesian coordinates with background flow velocity $V(x)\hat{\mathbf{e}}_y$, the dynamical u -moment equations for shear flow are

$$\frac{\partial}{\partial t} \left\langle \frac{\rho u_X^2}{2} \right\rangle + \nabla \cdot \left\langle \frac{1}{2} \rho u_X^2 \mathbf{u} \right\rangle = - \left\langle u_X \frac{\partial P}{\partial x} \right\rangle - \text{losses} \quad (6)$$

and

$$\frac{\partial}{\partial t} \left\langle \frac{\rho u_Y^2}{2} \right\rangle + \nabla \cdot \left\langle \frac{1}{2} \rho u_Y^2 \mathbf{u} \right\rangle = -\frac{dV}{dx} T_{XY} - \left\langle u_Y \frac{\partial P}{\partial y} \right\rangle - \text{losses} \quad (7)$$

where T_{XY} is the obvious analogue to $T_{R\phi}$.

In both disk and shear flow, the shear is the source of free energy which maintains the kinetic energy of the fluctuations. But the dynamical content of (6) and (7), as compared with (4) and (5) is evidently very different. The disk is faced with grave difficulties in keeping up both outward transport ($T_{R\phi} > 0$) and significant levels of $\langle u^2 \rangle$. Whereas $2\Omega T_{R\phi}$ is a source term for $\langle \rho u_R^2/2 \rangle$ if $T_{R\phi} > 0$, the $-\kappa^2/2\Omega$ term in equation (5) is a sink for $\langle \rho u_\phi^2/2 \rangle$. The presence of both a source and a sink coupled to $T_{R\phi}$ means that the u_R and u_ϕ fluctuations cannot grow simultaneously: one would grow only at the expense of the other, and the implicit correlation embodied in $T_{R\phi}$ could not be self-consistently maintained. One could appeal to the pressure term in equation (5) for help, and one needs to do so in *any* hydrodynamical disk flow where there is outward transport. This leads not to turbulence, whose physical origin is vorticity entrainment in large scale shear (Tennekes & Lumley 1972), but to transport by spiral waves. In shear flow there is no T_{XY} sink in the corresponding equation (7), and hence no barrier to maintaining both transport and fluctuation amplitude. The nonlinear instability (at sufficiently high Reynolds numbers) and resulting turbulence of simple shear flow is a matter of common experience. The behavior of disks could not be more different.

3. Numerical Procedure

Numerical simulations demonstrate the behaviors of disk and shear flows unambiguously. It is sufficient to work in the local shearing-periodic box system (Hawley, Gammie & Balbus 1995). The background angular velocity of the disk is taken to be a power law: $\Omega \propto R^{-q}$. We construct a set of local coordinates corotating with the fluid at a fiducial radius R_o . Equations are expanded to first order about R_o , using locally Cartesian coordinates $\mathbf{x} = (x, y, z) = (R - R_o, R_o(\phi - \Omega t), z)$. (Ω is evaluated at $R = R_o$ in the expression for y .) Although the local geometry is Cartesian, Coriolis and tidal forces ensure the local dynamics is not.

The resulting hydrodynamic equations are

$$\frac{\partial \rho}{\partial t} + \nabla \cdot (\rho \mathbf{v}) = 0, \quad (8)$$

$$\frac{\partial \mathbf{v}}{\partial t} + \mathbf{v} \cdot \nabla \mathbf{v} = -\frac{1}{\rho} \nabla P - 2\Omega \times \mathbf{v} + 2q\Omega^2 x \hat{\mathbf{x}}, \quad (9)$$

$$\frac{\partial \rho \epsilon}{\partial t} + \nabla \cdot (\rho \epsilon \mathbf{v}) + P \nabla \cdot \mathbf{v} = 0, \quad (10)$$

where the pressure P is given by the

$$P = \rho \epsilon (\gamma - 1), \quad (11)$$

and the remainder of the terms have their usual meaning. For simplicity, the vertical component of gravity is not included. The shearing box is defined to be a cube with length L ($= 1$) on a side, and the initial equilibrium solution is $\rho = 1$, $P = L\Omega^2$, and $\mathbf{v} = -q\Omega x \hat{\mathbf{y}}$.

The boundary conditions in the angular (y) and vertical (z) directions are strictly periodic. The radial (x) direction, however, is “shearing periodic.” This means that

the radial faces are joined together in such a way that they are periodic at $t = 0$ but subsequently shear with respect to one another. Thus, when a fluid element moves off the outer radial boundary, it reappears at the inner radial boundary at its appropriate sheared position, with its angular velocity compensated for the uniform mean shear across the box. See Hawley, Gammie, & Balbus (1995) for a detailed description of these boundary conditions.

To begin a simulation, a background angular velocity gradient (q value) is chosen, and initial velocity perturbations are introduced into the flow. Stability is determined by whether or not these fluctuations grow in amplitude. The simulations of BHS began with random perturbations in pressure and velocity applied as white noise down to the grid scale. However, such initial conditions have the disadvantage of varying with resolution; the initial perturbation spectrum will never be fully resolved. For the models computed in this paper, we use a specific initial perturbation rather than random noise. The initial conditions consist of well-defined products of sine-wave perturbations of v_y in all three spatial directions, with wavelengths L , $L/2$, $L/3$ and $L/4$. A linear combination of sine waves is constructed for each direction, e.g., if

$$f(x) = [\sin(2\pi x + \phi_1) + \sin(4\pi x + \phi_2) + \sin(6\pi x + \phi_3) + \sin(8\pi x + \phi_4)] \quad (12)$$

where the ϕ terms are fixed phase differences, then the perturbation is applied to v_y as

$$\delta v_y = AL\Omega f(x)f(y)f(z) \quad (13)$$

The amplitude A of the perturbation is set to some fraction of the shearing velocity $L\Omega$, typically 10%. This procedure ensures that the initial conditions will be the same for all simulations within a comparison group, regardless of grid resolution, and that they will be adequately resolved, even on the 32^3 zone grid.

Most of the simulations described in §4 were computed with the same code used in BHS. This is an implementation of the hydrodynamic portion of the ZEUS algorithm (Stone & Norman 1992). To address the possibility of numerical artifacts affecting our findings, it has proven useful to compare the results obtained using two very different numerical algorithms. To this end, we have adapted the Virginia Hydrodynamics-1 (VH1) Piecewise Parabolic Method (PPM) code to the three-dimensional shearing box problem. The PPM algorithm was developed by Colella & Woodward (1984), and it is a well-known, widely-used, and well-tested numerical technique for compressible hydrodynamics. Like ZEUS, PPM employs directional splitting, but differs fundamentally from ZEUS in its use of a nonlinear Riemann solver rather than finite differences to obtain the source terms in the Euler equations. PPM also uses piecewise parabolic representations (third order in truncation error) for the fundamental variables rather than the piecewise linear functions used in ZEUS (second order). Both schemes employ monotonicity filters to minimize zone to zone oscillations. VH1 uses a Lagrangian-remap approach in which each one-dimensional sweep through the grid is evolved using Lagrangian equations of motion, after which the results are remapped back onto the original grid using parabolic interpolations. Further information about the VH1 implementation of PPM is currently available at <http://wonka.physics.ncsu.edu/pub/VH-1>, and at <http://www.pbm.com/~lindahl/VH-1.html>.

4. Results

4.1. Flows Marginally Stable by the Rayleigh Criterion

A constant angular momentum distribution ($q = 2$) is marginally stable to linear perturbations by the Rayleigh criterion. BHS showed that such a flow, which has a vanishing epicyclic frequency, is formally equivalent in its stability properties to simple Cartesian shear. When $\kappa = 0$ equations (4) and (5) have the same form as (6) and (7). This equivalence implies that constant angular momentum flows should be subject to the same nonlinear instabilities that disrupt shear flows. The simulations of BHS demonstrate this unequivocally.

It is possible to explore deeper consequences of the symmetry. Not only should a $q = 2$ flow be formally analogous to a shear layer, a “ $q = 2 - \epsilon$ ” Rayleigh-stable flow should be formally analogous to a shear layer with a little bit of rotation: $d\Omega/d\ln R \gg 2\Omega$. This can be inferred from the $R \leftrightarrow \phi$ symmetry of equations (4) and (5). (From the standpoint of a source of free energy there is no problem; differential rotation serves this role. This is somewhat unusual, since normally the source of free energy disappears with the onset of linear stability.) At large Reynolds numbers, only the ratio of the coefficients of $T_{R\phi}$ matters, and where stability is concerned, reciprocal flows (those whose coefficient ratios are reciprocals of one another) should have the same stability properties. The $q = 2 - \epsilon$ case is important, because some Couette flows in which the outer cylinder dominates the rotation are found to be nonlinearly unstable, with the onset of instability occurring near the inner cylinder (Coles 1965; Drazin & Reid 1981). This breakdown is the basis of “subcritical” behavior, which is occasionally cited as evidence for nonlinear instability in *Keplerian* disks (e.g., Zahn 1991). From the symmetry reasons stated above, however, we believe that subcritical behavior is evidence that disks with $q = 2 - \epsilon$ are nonlinearly unstable, not $q = 1.5$ disks. This is a very testable hypothesis.

We examine this conjecture by computing models at 64^3 and 32^3 resolution, $1.94 \leq q \leq 2$ in intervals of 0.01, for two different amplitudes of initial perturbations: $\delta v_y = 0.1(L\Omega)$ and $\delta v_y = 0.01(L\Omega)$. The value of q determines the strength of the linear stabilization, the initial perturbation amplitude sets the strength of the initial nonlinear interactions, and the grid resolution influences the amount of stabilizing numerical damping present [“losses” in (4) and (5)]. Together these effects will determine when the perturbations grow and when they do not.

Figure 1 displays some of the results. Figure 1a shows the perturbed kinetic energy in units of $L\Omega$ for the 32^3 resolution, large amplitude ($\delta v_y = 0.1L\Omega$) perturbation models. The different q models begin with the same initial perturbations of the form (13). The kinetic energy decreases during the first orbit, and the curves promptly separate according to angular momentum distribution, with the smallest q model decaying the most rapidly. Only the flows with $q = 2$ and 1.99 show any subsequent growth. The $q = 1.98, 1.97, 1.96$ and 1.95 models die away; the smaller the value of q , the lower the remaining kinetic energy. Figure 1b depicts models with the same range of q and the same initial perturbations, but computed with 64^3 grid zones. Again there is a short initial period of rapid decline in perturbed kinetic energy, with the curves separating according to q . However, this decrease is smaller than that seen in the 32^3 zone simulations. After about one orbit in time, the kinetic energies grow for all but the $q = 1.96$ and 1.95 model. These models vary with time around an average that remains close to the initial value; only the $q = 1.94$ model experiences a clear decline in perturbed kinetic energy with time.

The sensitivity of the nonlinear instability to initial perturbation amplitudes is

demonstrated with a third group of 64^3 grid zone models. These are begun with an initial perturbation amplitude of only $\delta v_y = 0.01L\Omega$ (Fig. 1c). The perturbation kinetic energy increases slightly during the first orbit, and again the curves separate according to q value. In this case, however, only the $q = 2.0$ model shows growth; all the others die away.

Because the instability is truly nonlinear, the details of how a flow develops depend upon the amplitude of the initial disturbance, and, to a far greater degree than for a linear instability, the numerical resolution. When $\kappa^2 = (2 - q)\Omega = 0$ the linear forces on the system sum to zero, and nonlinear dynamics determine the fate of the flow. The simple shear flow shows that in the absence of a restoring force the nonlinear dynamics are destabilizing. As κ^2 slowly increases from zero, the linear restoring force returns; the separation of the curves by q value illustrates the stabilizing effect of the Coriolis force. Whether or not the linear restoring force can ensure stability in a given system depends on its strength compared to that of the nonlinear dynamics, which, in turn, depend on the amplitude of the initial perturbations. The larger the perturbations, the greater the nonlinear forces.

The subcritical behavior of $2 - \epsilon$ flows seems to have its roots in epicyclic excursions. The mechanism of instability in planar Couette flow is believed to be vorticity stretching in the shear (Tennekes & Lumley 1972). The presence of epicyclic motion in general is incompatible with this process. Nearby perturbed elements execute bound (pressure modified) epicyclic orbits around a common angular momentum center. There is no indefinite stretching of local vortices, or at least the process is far less efficient. But the aspect ratio of the ellipse epicycle becomes extreme as $q \rightarrow 2$; in the absence of pressure, the minor to major (radial to azimuthal) axis ratio for displacements in the disk plane is $(1 - q/2)^{1/2}$. At some point, it is all but impossible to distinguish the epicycle from the shearing background, and of course the epicyclic frequency is then tiny compared with the shearing rate. This latter rate is the time scale for vortex stretching, and so we expect this mechanism for turbulence to be viable under these conditions. The fact the formal linear epicyclic excursion may be bound is inconsequential. Vortex stretching and the feeding of turbulence will proceed if there is ample time before the epicycle closes. For $q = 1.95$, the approximate threshold for nonlinear instability found in the simulations, $\kappa = 0.2|d\Omega/d \ln R|$, and the aspect ratio quoted above is 0.16, i.e. about 6 to 1 major to minor axis ratio. These are sensible values in the scenario we have suggested: if κ is not less than an order of magnitude smaller than the shearing rate, or the aspect ratio is not less than 0.1 to 0.2, then the flow is strongly stabilized by Coriolis-induced epicyclic motion. In this case, vortices are not stretched efficiently by the background shear: rather than monotonically increasing the distortion, the epicyclic orbit relaxes the vortex stretching over half of the period.

Numerical diffusion error represents a loss term from (4) and (5), and this adds to the stabilizing effect by reducing the amplitude of the perturbations. At a given resolution, however, numerical effects should be nearly the same from one q value to the next. Hence a series of models that differ by only q isolates the physical effects from the numerical. Any differences observed in these simulations are dynamical, not numerical, in origin.

To conclude, we have observed that the growth or decay of applied velocity perturbations depends on the resolution and the initial perturbation amplitude for flows near the critical $\kappa^2 = 0$ limit. This hypersensitivity, however, is shown only over a tiny range of q . Below $q = 1.95$ all indications of instability are gone. These results are precisely what one would expect from the presence of a nonlinear instability, and they are consistent with the observed presence of such instabilities in shear dominated, but formally Rayleigh-stable

Couette experiments.

4.2. The Influence of Resolution and Algorithm

A concern in any numerical study, particularly one whose goal is to search for a physical instability, is the effect of finite numerical resolution. In §4.1 we demonstrated how various flows could be stabilized by increasing the epicyclic frequency (through a decrease in q from the critical value of 2.0). In some of these cases, a transition from stability to instability occurred when resolution was increased. Clearly, numerical resolution does play its anticipated role: numerical diffusion error has a stabilizing effect. But is numerical diffusion error decisive as q becomes smaller?

BHS argued that the stability of Keplerian flow to finite perturbations was due to physical, not numerical effects, and gave support to that position through simulations done at three resolutions, all of which produced similar results. In this section we describe a series of simulations that improve upon those previous resolution experiments. We have evolved a series of Keplerian flows with a range of numerical resolutions. We begin with 32^3 grid zones, and then increase the number of grid zones by a factor of two in each of the three dimensions in subsequent simulations, up to 256^3 grid zones. Each of these Keplerian flows is perturbed with angular velocity fluctuations of the form (13), with an maximum initial amplitude of $\delta v_y = 0.1L\Omega$.

Figure 2 shows the evolution of the kinetic energy of the angular and radial velocity perturbations, $(\rho v_x^2)/2$ (Fig. 2a) and $(\rho \delta v_y^2)/2$ (Fig. 2b). The initial perturbations produce radial kinetic energies which rapidly (0.2 orbits) increase to a maximum value comparable with the azimuthal component. Beyond this point, the perturbed kinetic energies drop off with time; the higher the resolution, the less rapid the decline, although each doubling in resolution creates a diminishing change. All resolutions show rapid decrease in $(\rho \delta v_y^2)/2$ from the initial value. One intriguing difference between the models is that the higher the resolution, the *lower* the value of $(\rho \delta v_y^2)/2$ after about 2 orbits. Thus, far from promoting greater instability, higher resolution is *reducing* the amplitude of the angular momentum perturbations.

Why should an increase in resolution lead to more rapid damping? This is clearly at variance with the expected behavior if numerical diffusion were the sole sink of perturbed kinetic energy. As we have emphasized, there is also a significant dynamical sink. Equation (5) shows that the Reynolds stress is a loss term for $\langle \delta v_y^2 \rangle$. All simulations begin with a positive Reynolds stress, and the higher resolution simulations maintain larger values during the initial orbit. At each resolution, the Reynolds stress can be integrated over time and space to give a measure of its strength: $\int \frac{\kappa^2}{2\Omega} \langle \rho v_x v_y \rangle dt$. These values *increase* monotonically with resolution, from 0.0033, to 0.0059, 0.0078, and finally to 0.0092 for the 256^3 model. (For reference, the initial value of $\langle \frac{1}{2} \rho v_y^2 \rangle$ is 0.04.)

Further evidence for the damping effect of the Reynolds stress can be seen in the low resolution run. In Figure 3 we plot $(\rho \delta v_y^2)/2$ (Fig. 3a) and the Reynolds stress (Fig. 3b) as a function of time for the first orbit in the 32^3 grid zone model. This low resolution simulation is of special interest because at orbit 0.25 the averaged Reynolds stress becomes negative. At the same time, the rate of decline of $\langle \rho \delta v_y^2 \rangle$ decreases, as one would anticipate

from (5). Hence, although at low resolution grid scale numerical diffusion is the largest loss term in the angular velocity fluctuation equation, the sink due to the Reynolds stress is large enough to observe directly. Improved numerical resolution increases the dynamical Reynolds sink by a greater factor than it reduces the numerical diffusion!

We next turn to simulations of Keplerian flows at 32^3 , 64^3 and 128^3 grid zone resolutions using the VH1 PPM code. We ran the same problem with the same initial perturbations as above. Figure 4 shows the time-history of the perturbed radial and azimuthal kinetic energies. This plot should be compared with Figure 2 and for reference we include the 32^3 and the 128^3 ZEUS simulation results as dashed lines. Figure 5 is the Reynolds stress during the first orbit for all the resolutions and for both algorithms; the PPM runs are the bold lines.

The PPM results are completely consistent with the ZEUS simulations. Most striking is the close similarity between a given PPM evolution and the ZEUS simulation run at twice its resolution. For example, the history curve of the Reynolds stress in the PPM 32^3 run lies almost on top of the ZEUS 64^3 curve (fig. 5) through 0.2 orbits in time. The Reynolds stresses in the 64^3 and 128^3 PPM simulations peak at the same level as the 256^3 ZEUS simulation, then decline at slightly different rates beyond 0.2 orbits. The 128^3 PPM simulation apparently has less numerical diffusion than the 256^3 ZEUS model. Regardless of the relative merits of the two schemes, the succession of curves with increasing resolution showing the same outcome, done with two completely independent algorithms, indicates convergence to a solution near that of the maximum resolution models. In other words, Keplerian disks would prove stable even if computed at arbitrarily high resolution.

4.3. Nonlinear Decay in the Keplerian System

In simulations of Keplerian differential rotation, the kinetic energy of the perturbations declines at a rate which itself decreases with time. Why should there be any decay at all in a stable inviscid system? Is this decay entirely a numerical artifact?

These simulations begin with perturbations of the form (13). The initial power spectrum for the perturbed kinetic energy thus contains power in the first four wavenumbers only. Once the evolution begins, nonlinear interactions cause a cascade of available perturbed kinetic energy into higher wavenumbers. Dissipation occurs rapidly at the highest wavenumber. Although this dissipation is numerical, it mimics the behavior of physical dissipation at the viscous scale. The rate at which energy cascades to larger wavenumbers, and hence the rate at which the perturbed kinetic energy declines, should again be a function of numerical resolution and perturbation amplitude. In this section we investigate these effects, explore the reasons for the decay of the turbulence, and examine the properties of the velocity fluctuations that remain at late time.

A study the Fourier power spectrum of the perturbed kinetic energy yields important information. Because the background velocity has shear, we must transform the data into coordinates in which the shearing box system is strictly periodic, take the Fourier transform, and then remap the wavenumbers onto the fixed Eulerian system. This procedure is described in Hawley et al. (1995). Figure 6 is a one dimensional power spectra, $|\delta\mathbf{v}(k)|^2$ in k_x , k_y , and k_z , for the 64^3 and 128^3 grid zone Keplerian PPM simulations discussed in §4.2. The spectra are shown for orbits 1, 2 and 3, with the dashed lines corresponding to the 64^3

run and the solid lines to the 128^3 model. The initial perturbation spectrum is constant across the first four wavenumbers (seen in Figure 6 as a horizontal line).

Immediately after the evolution begins, energy cascades into higher wavenumbers. Within one third of an orbit, a relatively smooth power law distribution has been established. As time goes by the energy at all wavenumbers steadily declines. The power spectrum across the smallest wavenumbers remains relatively flat but has dropped steadily from $t = 0$. Beyond $k \sim 10$ the spectra drop off as steep power laws, with the k_y distribution the steepest of all three directions. Because of the background shearing velocity, transport in y direction produces the largest numerical diffusion. The k_x function has the smallest slope. In this case, the background shear causes low k_x waves to be wrapped into higher wavenumbers, i.e., $k_x(t) = k_x(0) - tmd\Omega/dR$, where m is an azimuthal wavenumber. The higher resolution curves in Figure 6 have larger energies compared to the low resolution curve. Aside from this, the additional grid zones extend the curves out to higher wavenumber without much significant qualitative difference.

Next we consider the effect of the initial perturbation amplitude on the rate of decay of the turbulence and the properties of the system at late times. Experience suggests that if a system is vulnerable to nonlinear instabilities, large initial perturbation amplitudes will promote the onset of turbulence. Indeed, this is what was observed in the marginally Rayleigh-stable runs described in §4.1. Here we run a series of low resolution 32^3 Keplerian simulations that have initial velocity perturbations with maximum values equal to $\delta v_y/L\Omega = 1.0, 0.1, 0.01$, and 0.001 . The time evolution of the perturbed kinetic energies in these four runs is shown in Figure 7. All the runs show rapid decay; contrary to naive expectations, however, the higher the initial perturbation amplitude the *larger* the initial decay rate of the perturbed kinetic energy.

Figure 8 illustrates the reasons for this. Figure 8 shows the 1D Fourier power spectrum for the largest and smallest initial perturbation runs after 0.25 orbits. The importance of nonlinear interactions is increased by larger initial amplitudes. This is why in §4.1 nonlinear effects were able (in some cases) to overcome the stabilizing influence of the Coriolis force when the initial perturbation amplitudes were increased. Here, however, the main nonlinear effect promoted by increased perturbation amplitude is to create a more rapid cascade of energy to high wavenumbers. In contrast, the $\delta v_y = 0.001L\Omega$ case is dominated by linear and numerical effects. Energy has been carried into higher k_x wavenumbers by linear shear, and lost from k_y by numerical diffusion error. The spectrum in k_z is completely flat through the first four wavenumbers (those initially powered) before dropping precipitously.

Evidence for a strong nonlinear cascade in the largest initial perturbation runs is also found in the rapid increase in entropy at the start of the evolution due to thermalization of the initial kinetic energy in those runs. By orbit 5, the decay rates have been reduced to a much lower level comparable to that seen in the small amplitude perturbation runs. The ratio of the kinetic energy at orbit 5 to the initial value in each of these runs is 0.00042, 0.0042, 0.014, and 0.058. Eventually the fluctuation energy in all these simulations levels off at a finite, small value. What remains at these late times are pressure and epicyclic waves, whose amplitude is determined by the strength of the initial perturbation. The very slow numerical decay of these long-wavelength linear waves is due to numerical dissipation. The Reynolds stress oscillates around zero in all runs, with an amplitude similar to the late-time kinetic energy.

We have argued that the residual kinetic energy represents nothing more than linear waves left over from the initial perturbations. Their presence does not imply that Keplerian

disks are somehow still “slightly unstable”; stability certainly does not require that velocity perturbations die out. Indeed, a complete decay to zero amplitude would have been puzzling; the motivation of the section after all was to give an account of why there was *any* decay. This understood, even low levels of velocity fluctuations might be of interest in a disk, if they could be sustained indefinitely. Can one convincingly rule out the possibility that these lingering fluctuations are somehow feeding off the differential rotation? An experiment to test this conjecture is to chart the evolution of perturbations in a $q = 0$, constant Ω flow. In a uniformly rotating disk, Coriolis forces are present without any background shear at all. Such a system is rigorously stable; without background shear there is no source of energy to feed velocity perturbations. At late times, the noise in a uniformly rotating disk must reflect residual energy from the initial conditions, not ongoing excitation. Further, the absence of shear flow will reduce the effective numerical viscosity; the perturbations will not be advected by the shear flow, nor will radial wavenumber modes be sheared out to higher values.

The $q = 0$ case has been run at two resolutions, 64^3 and 32^3 , for comparison with equivalently resolved Keplerian systems. The initial perturbations have a maximum value $\delta v_y = 0.1L\Omega$. The time histories of the perturbed kinetic energy for both the $q = 0$ and the $q = 1.5$ 64^3 simulations are shown in Figure 9. Both angular velocity distributions show rapid declines in kinetic energy, although after 10 orbits the rate of decline is greatly reduced. The 32^3 resolution simulations look similar, except that they have less energy at late time. The residual energy is due to stable waves that have not yet been damped by numerical diffusion. Compared to similarly resolved simulation with a Keplerian rotation profile ($q = 1.5$) the $q = 0$ models level out at *higher* energies. Without advection through the grid, there is less numerical diffusion, and higher residual wave amplitudes are preserved. The case for driven residual weak Keplerian turbulence becomes untenable, if the “turbulence” is stronger in a rigorously stable uniformly rotating disk!

4.4. The Contrast with Magnetic Turbulence

Although Keplerian flows have proven to be stable to the local development of hydrodynamic turbulence, the inclusion of a magnetic field changes everything, even if the field is weak (subthermal). Hydrodynamic stability in a differentially rotating system is assured so long as the Rayleigh criterion $dL/dR > 0$ is satisfied. Magnetic differentially rotating systems quite generally require $d\Omega/dR > 0$ for stability (Balbus 1995), a condition not satisfied in accretion disks. With a magnetic field present the stress tensor acquires a magnetic component proportional to $B_R B_\phi$,

$$T_{R\phi} = \langle \rho u_R u_\phi - \rho u_{AR} u_{A\phi} \rangle, \quad (14)$$

where

$$\mathbf{u}_A = \frac{\mathbf{B}}{\sqrt{4\pi\rho}}. \quad (15)$$

Most importantly, the way the stress tensor couples to the fluctuations changes. With the new expression for $T_{R\phi}$ the mean flow equations (2) and (3) are unchanged, but the fluctuation equations become

$$\frac{1}{2} \frac{\partial}{\partial t} \langle \rho(u_R^2 + u_{AR}^2) \rangle + \nabla \cdot \langle \quad \rangle = 2\Omega \langle \rho u_R u_\phi \rangle - \langle u_R \frac{\partial P_{tot}}{\partial R} \rangle - \text{losses}, \quad (16)$$

$$\frac{1}{2} \frac{\partial}{\partial t} \langle \rho(u_\phi^2 + u_A^2) \rangle + \nabla \cdot \langle \quad \rangle = -2\Omega \langle \rho u_R u_\phi \rangle - T_{R\phi} \frac{d\Omega}{d \ln R} - \left\langle \frac{u_\phi}{R} \frac{\partial P_{tot}}{\partial \phi} \right\rangle - \text{losses}. \quad (17)$$

(Terms proportional to $\nabla \cdot \mathbf{u}$ have been dropped, the fluxes are not shown explicitly, and $P_{tot} = P + B^2/8\pi$.)

Now the stress tensor no longer works at cross purposes to itself. There is still Coriolis stabilization in equation (17), but it is not sufficient to overcome the stress–gradient coupling term. One consequence of this is the now well-understood linear instability of weak magnetic fields in disks (Balbus & Hawley 1991; see reviews by Papaloizou & Lin 1995, and Balbus & Hawley 1998). Another is that outward transport of angular momentum maintains the turbulence self-consistently by directly tapping into the free energy of differential rotation.

The different couplings of the Maxwell (magnetic) and Reynolds stresses can be demonstrated in simulations. Abramowicz, Brandenburg, & Lasota (1996) carried out a series of simulations with different values of background q . They found an increase in angular momentum transport levels roughly in proportion to the background shear to vorticity ratio, i.e., $q/(2 - q)$. This result is best understood by rewriting the right hand side of (17) to obtain

$$\frac{1}{R} \frac{dR^2\Omega}{dR} \langle \rho u_R u_\phi \rangle - \frac{d\Omega}{d \ln R} \langle \rho u_{AR} u_{A\phi} \rangle. \quad (18)$$

Thus the Reynolds (kinetic) stress couples directly to the vorticity $[= (2 - q)\Omega]$, and the Maxwell (magnetic) stress couples to the shear ($q\Omega$). In other words, vorticity limits turbulence whereas shear promotes it.

Here we expand the study of Abramowicz et al. by examining a full range of q values between 0 and 2 in intervals of 0.1 in a local shearing box. The simulations are of the same type as some of those presented in Hawley, Gammie & Balbus (1996). The initial magnetic field is $B_z \propto \sin(2\pi x/L_x)$ with a maximum corresponding to $\beta = P/P_{mag} = 400$. The box size is $L_x = L_z = 1$, and $L_y = 2\pi$, and the grid resolution is $32 \times 64 \times 32$.

Figure 10 shows time-averaged Reynolds and Maxwell stresses as a function of q for the full range of simulations. The magnetic instability is present for all $q > 0$. Equation (18) provides no direct limit on the Maxwell stress; it acquires whatever level the nonlinear saturation of the instability can support. However, if the turbulence is to be sustained from the differential rotation, not pressure forces, the Maxwell stress must in general exceed the Reynolds stress by more than $(2 - q)/q$, the ratio of the vorticity to the shear. In practice the ratio of the Maxwell stress to Reynolds stress is significantly greater than this, particularly in the range $0 < q < 1$. In this regime the vorticity is so strongly stabilizing that the Reynolds stress is kept to a minimum even when fluid turbulence is created and maintained by the magnetic instability. When $q > 1$, however, the shear and vorticity become comparable; the Reynolds and Maxwell stresses both climb with increasing q . As $q \rightarrow 2$, the vorticity goes to zero and there are no constraints on the Reynolds stress from (18). The total stress increases dramatically as the flow enters the domain of the nonlinear hydrodynamical instability. When $q > 2$, of course, the flow is Rayleigh unstable.

5. Discussion

In this paper we have carried out a series of numerical simulations to explore further the local hydrodynamical stability properties of Keplerian disks, and the role that the Reynolds stress plays in determining that stability. The key conceptual points are embodied in the moment equations (4) and (5) for hydrodynamics, and (16) and (17) for magnetohydrodynamics. The differences in those equations are clearly manifest in simulations, both hydrodynamic and MHD. The Maxwell stress couples to the shear, the Reynolds stress to the vorticity. While the former maintains turbulence, the latter works against it. Thus, while magnetized disks are unstable, and naturally create and sustain turbulence, a nonmagnetized Keplerian flow possesses only the Reynolds stress, and that cannot by itself sustain turbulence. The accumulating evidence, both numerical and analytic, from this paper and earlier works (BHS; Stone & Balbus 1996), points clearly to the conclusion that Keplerian flows are locally hydrodynamically stable, linearly and nonlinearly.

It has been traditional to point to the nonlinear instabilities observed in simple shear flows to support the conjecture that Keplerian disks behave similarly. Such reasoning, however, neglects the critical difference between such flows, namely the dynamical stabilization due to the Coriolis force. Linear stabilization is measured by the epicyclic frequency, $\kappa^2 = 2(2 - q)\Omega^2$. As $q \rightarrow 2$, $\kappa^2 \rightarrow 0$, and dynamical stabilization becomes weaker and weaker. At $q = 2$ it vanishes completely; the flow becomes equivalent to a simple Cartesian shear and subject to the nonlinear instabilities to which simple shear flows are prone. Viewed in this light, the nonlinear instability of a Cartesian shear flow is less a generic property than a singular case lying between the linearly unstable and linearly stable regimes. The nonlinear instability exists not because nonlinear forces can generally overcome linear restoring forces, but because those linear forces vanish at the delimiting boundary between Rayleigh stability ($q < 2$) and instability ($q > 2$).

This is highlighted by our study of the transition between stability and instability. By varying q to values near to but slightly less than 2, we can explore the dynamics of systems close to the marginal stability limit. We find that when stabilization from the Coriolis term is very weak, both the amplitude of the initial perturbations and the size of the numerical diffusion error (grid resolution) can determine whether the velocity perturbations amplify or decay. This is entirely consistent with the experimental configurations that are linearly stable but which nevertheless become unstable. Such nonlinearly unstable systems are precisely those where a large shear dominates over other factors (e.g., a rapidly rotating outer cylinder in a Couette experiment). In these fluid experiments the transition to turbulence depends on the amplitude of the perturbing noise and the Reynolds number of the flow. When we reduce the strength of the Coriolis force by varying q just below the marginally stable value $q = 2$, we produce a similar dominance of shear and again find an instability that depends on the initial perturbation amplitude and the (numerical) viscosity. We have understood this in terms of epicyclic orbits, which are highly distorted near $q = 2$, almost indistinguishable from background shear. Once q is sufficiently below $q = 2$, however, Coriolis stabilization is powerful, epicycles are rounder, and perturbation growth is no longer possible.

This conclusion is greatly strengthened by experiments in which the Keplerian system is evolved with different initial perturbations and different grid resolutions. First we explored the impact of finite resolution. Recall that the effect of numerical diffusion error on flow structure (the turbulent perturbations) will be as an additional loss term in (4)

and (5). Even if we were to assume an ideal scheme with no numerical losses, however, the sink due to the Coriolis term in (5) would remain unchanged. The simulations with various q values near but just below 2 provide a quantitative measure of just how big that term needs to be to stabilize the flow, and an estimate of the importance of numerical viscosity as a loss term. Although we find that increasing the effective Reynolds number (i.e., by increasing the resolution and thusly reducing numerical diffusion) can convert a marginally stable flow into a marginally unstable one, one should not conclude that further increases will have a similar effect on strongly stable Keplerian flows. Vortex stretching can “sneak” into a highly elongated epicycle, but it cannot do so in a rounded, strongly stable Keplerian disturbance.

We have investigated the possibility of diffusive numerical stabilization with a series of resolution experiments run with two completely different algorithms. Keplerian simulations were run at 4 resolutions from 32^3 up to 256^3 using the ZEUS hydrodynamics scheme, and 3 resolutions from 32^3 up to 128^3 using the PPM algorithm. The results from all these simulations were very similar. No hint of instability was seen in any of these simulations, nor was there any trend observed which could conceivably suggest instability in an extrapolation to arbitrarily high resolution. Furthermore, not just decaying trends, but detailed numerical behavior was reproduced in two distinct codes with very different numerical diffusion properties. The case that numerical diffusion is dominating and stabilizing these runs is untenable.

Next, a series of experiments explored a range of initial perturbation amplitudes. The largest had initial fluctuations that were comparable to the background rotation velocity $L\Omega$. We found that the *larger* the initial perturbation, the more rapid the decay of the resulting turbulence. Far from promoting instability, stronger initial perturbations actually increase the rate of decay of the perturbed kinetic energy. When finite amplitude perturbations are added to the Keplerian system they rapidly establish a nonlinear cascade of energy to higher wavenumbers. This energy is then thermalized (or lost, depending upon the numerical scheme and the equation of state) at the high wavenumber end. Linear amplitude perturbations do not decay via such a cascade, and damp at much lower rates.

Turbulence decays in homogeneous systems lacking an external energy source. A uniformly rotating disk is an example of such. A Keplerian system is more interesting because decay is observed despite the presence of free energy in the differential rotation which could, in principle, sustain the turbulence. This does not happen, however, because the coupling of the Reynolds stress to the background vorticity simply makes it impossible to power simultaneously both the radial and azimuthal velocity fluctuations that make up the Reynolds stress. Residual levels of fluctuations were even lower in the Keplerian disk than they were in the uniformly rotating disk.

This behavior stands in contrast to the MHD system. The magnetic instability produces not just turbulent fluctuations, but the *right kind* of fluctuations: positive correlations in u_R and u_ϕ , and in B_R and B_ϕ . It is because the magnetorotational instability is driven by differential rotation that the critical R – ϕ correlations exist. Unless $T_{R\phi}$ were positive, energy would not flow from the mean flow into the fluctuations. Hydrodynamical Cartesian shear flows maintain the correlation physically by ensnaring vortices (a nonlinear process); magnetic fields do this by acting like springs attached to the fluid elements (a linear process). Sources of turbulence other than the differential rotation (or simple shear) do not force a correlation between u_R and u_ϕ , and generally do not lead to enhanced outward transport.

Magnetic fields, then, are uniquely suited to be the agents responsible for the behavior of α disks. While this conclusion has important implications for fully ionized disks, its implications for protostellar disks are yet more profound. If such disks are unable to sustain adequate levels of magnetic coupling, or unable to sustain such coupling throughout their radial extent, angular momentum transport may well be tiny or nonexistent. Angular momentum transport, when it occurs, will have to be accomplished through global nonaxisymmetric waves, driven, for example, by self-gravitational instabilities. Even if triggered by, say, convective instability, turbulence would likely prove to be transient: it cannot be sustained from the only source of energy available, namely the differential rotation. More generally, nonmagnetic disks will not be describable in terms of the usual α model.

Phenomenologically much less is known of MHD turbulence than of hydrodynamical turbulence. There is very little laboratory to draw upon, in contrast to the rich literature of hydrodynamical Couette flow. The observational complexity of many disk systems suggests the presence of a versatile and eruptive source of turbulence; magnetic fields seem an obvious candidate for producing such behavior. The physics behind magnetic reconnection, large scale field topology, ion-neutral interactions, magnetic Prandtl number, and global dynamos is likely to prove at least as rich and complex as the behavior of astrophysical disks.

This work is supported in part by NASA grants NAG5-3058, NAG5-7500, and NSF grant AST-9423187. Simulations were carried out with support from NSF Metacenter computing grants at the Pittsburgh Supercomputing Center and at NPACI in San Diego.

References

- Abramowicz, M., A. Brandenburg, & J.-P. Lasota 1996, MNRAS, 281, L21
- Balbus, S. A. 1995, ApJ, 453, 380
- Balbus, S. A., & Hawley, J. F. 1991, ApJ, 376, 214
- Balbus, S. A., & Hawley, J. F. 1998, Rev Mod Phys, 70, 1
- Balbus, S.A., Hawley, J.F., & Stone, J.M. 1996, ApJ, 467, 76 (BHS)
- Cabot, W. 1996, ApJ, 465, 874
- Cameron, A. G. W. 1978, Moon and Planets, 18, 5
- Colella, P., & Woodward, P. R. 1984, J. Comput. Phys., 54, 174
- Coles, D. 1965, J. Fluid Mech, 21, 385
- Crawford, J. A., & Kraft, R. P. 1956, ApJ 123, 44
- Cuzzi, J. N., Dobrovolskis, A. R., & Hogan, R. C. 1996, in Chondrules and the Protoplanetary Disk, ed. R. H. Hewins, R. H. Jones, & E. R. D. Scott (Cambridge: Cambridge Univ. Press), 35
- Drazin, P. G., & Reid, W. H. 1981, Hydrodynamical Stability (Cambridge: Cambridge University Press)
- Hawley, J. F., Gammie, C. F., Balbus, S. A. 1995, ApJ, 440, 742
- Hawley, J. F., Gammie, C. F., Balbus, S. A. 1996, ApJ, 464, 690
- Kley, W., Papaloizou, J. C. B., & Lin, D. N. C. 1993, ApJ, 416, 679
- Lin, D. N. C., & Papaloizou, J. C. B. 1980, MNRAS, 191, 37
- Papaloizou, J. C. B., & Lin, D. N. C. 1995, ARAA, 33, 505
- Prinn, R. G. 1990, ApJ, 348, 725
- Ryu, D. & Goodman, J. 1992, ApJ 388, 438
- Shakura, N. I., & Sunyaev, R. A. 1973, A&A, 24, 337
- Stone, J. M., & Balbus, S. A. 1996, ApJ, 464, 364
- Stone, J. M., & Norman, M. L. 1992, ApJS, 80, 753
- Tennekes, H., & Lumley, J. L. 1972, A First Course in Turbulence (Cambridge: MIT Press)
- Zahn, J-P. 1991, in Structure and Emission Properties of Accretion Disks, C. Bertout, S. Collin-Souffrin, J-P. Lasota, & J. Tran Thanh Van eds (Gif sur Yvette, France: Editions Frontières)

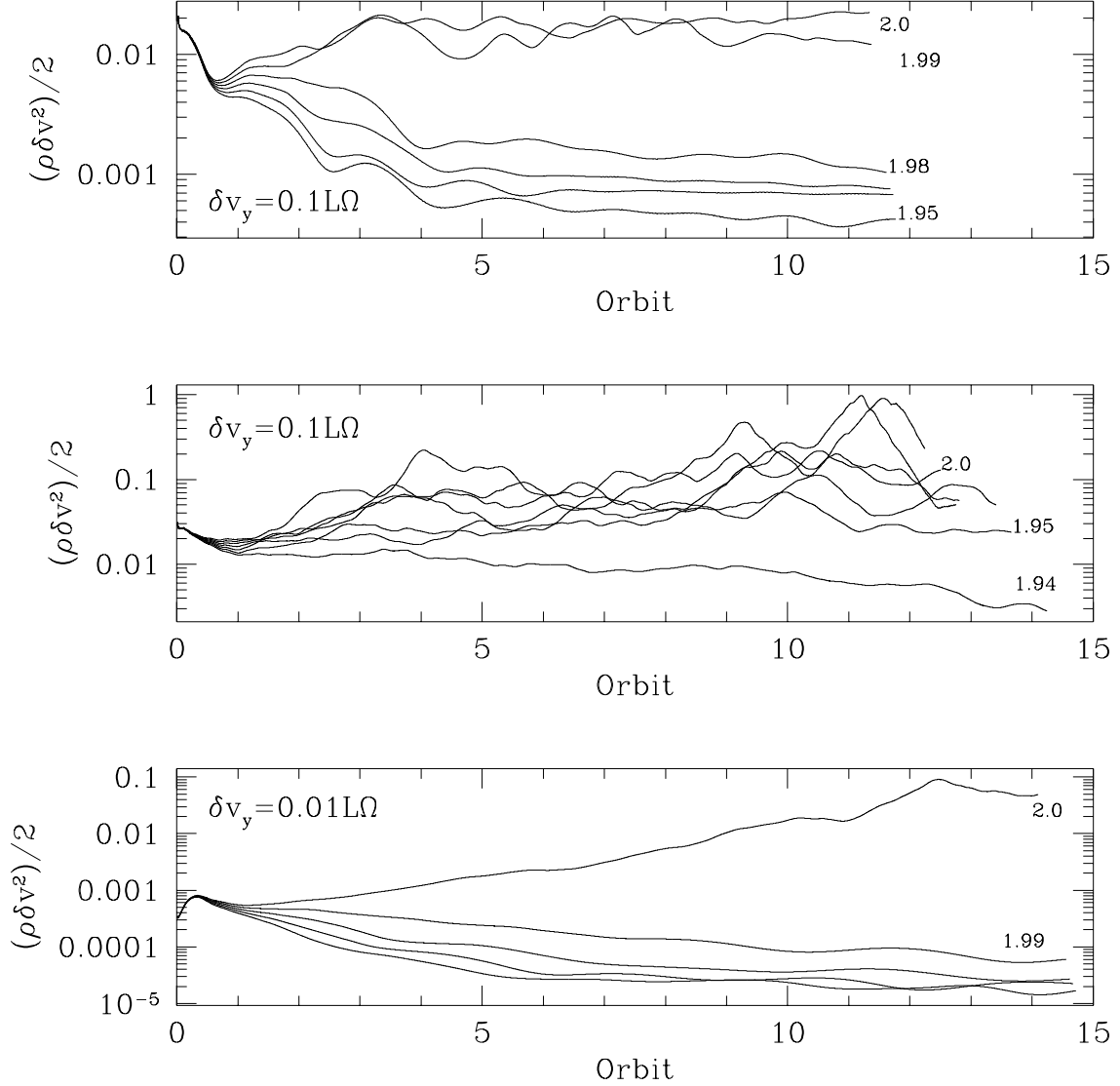


Fig. 1.— Evolution of kinetic energy of velocity perturbations for background rotation laws $\Omega \propto R^{-q}$ near the marginally stable constant angular momentum distribution $q = 2$. Selected curves are labeled by their q value. Top: Low resolution 32^3 grid zone simulations with initial maximum perturbation $\delta v_y = 0.1 L \Omega$. Only the upper two curves ($q = 2$ and $q = 1.99$) show any perturbation amplification. Middle: Simulations with 64^3 grid zone resolution and initial perturbation amplitude $\delta v_y = 0.1 L \Omega$. The 6 curves correspond to $q = 2.0$ to $q = 1.94$ in increments of 0.01. The $q = 1.95$ curve remains level while the $q = 1.94$ declines with time. Bottom: Simulations with 64^3 grid zones and initial perturbation amplitude $\delta v_y = 0.01 L \Omega$. There 5 curves range from $q = 2.0$ to $q = 1.96$ in increments of 0.01. Only the $q = 2.0$ curve shows growth.

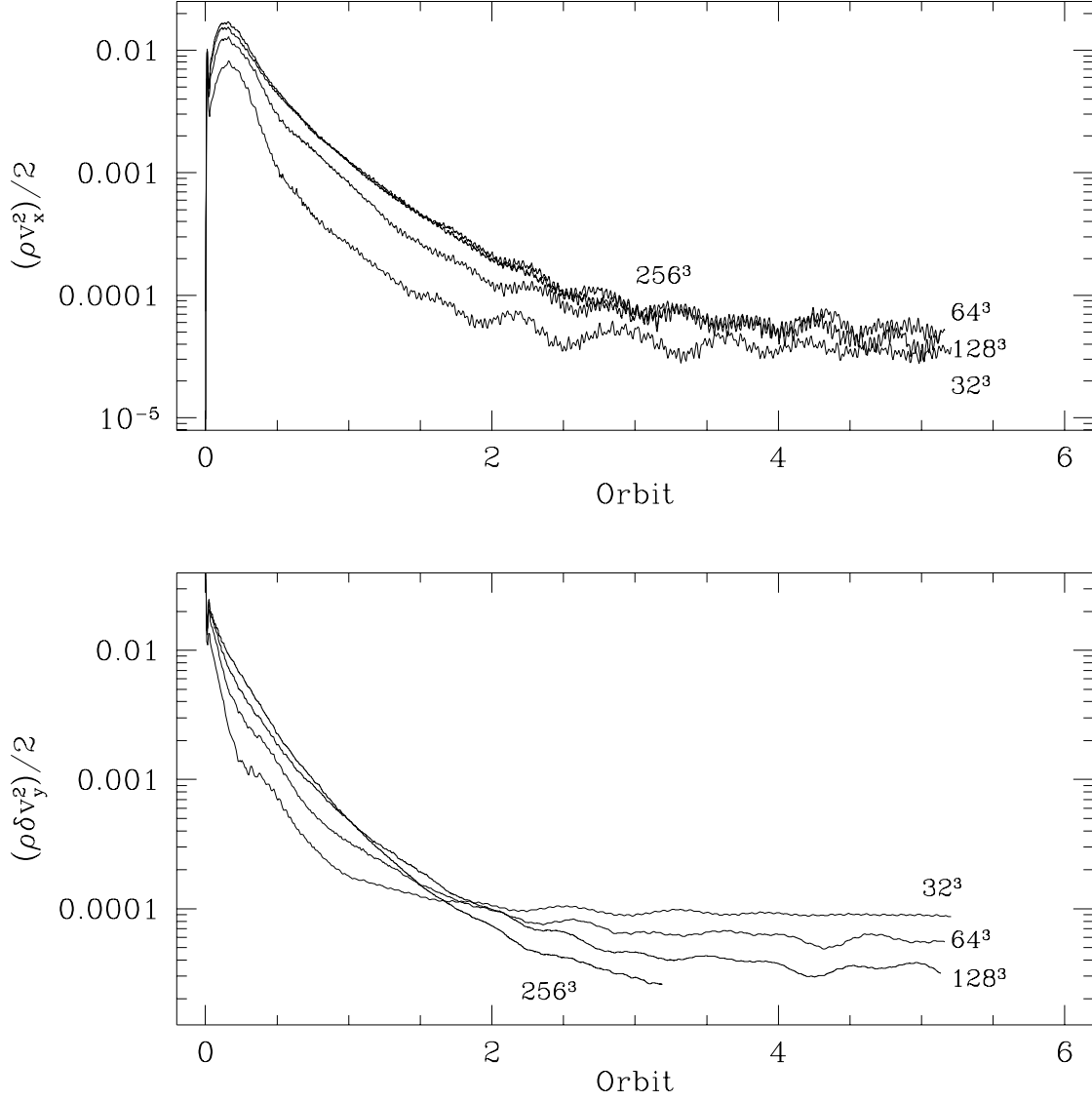


Fig. 2.— Evolution of v_x (top) and v_y (bottom) fluctuation kinetic energy for simulations with resolutions of 32^2 , 64^3 , 128^3 , and 256^3 grid zones. Curves are labeled by resolution.

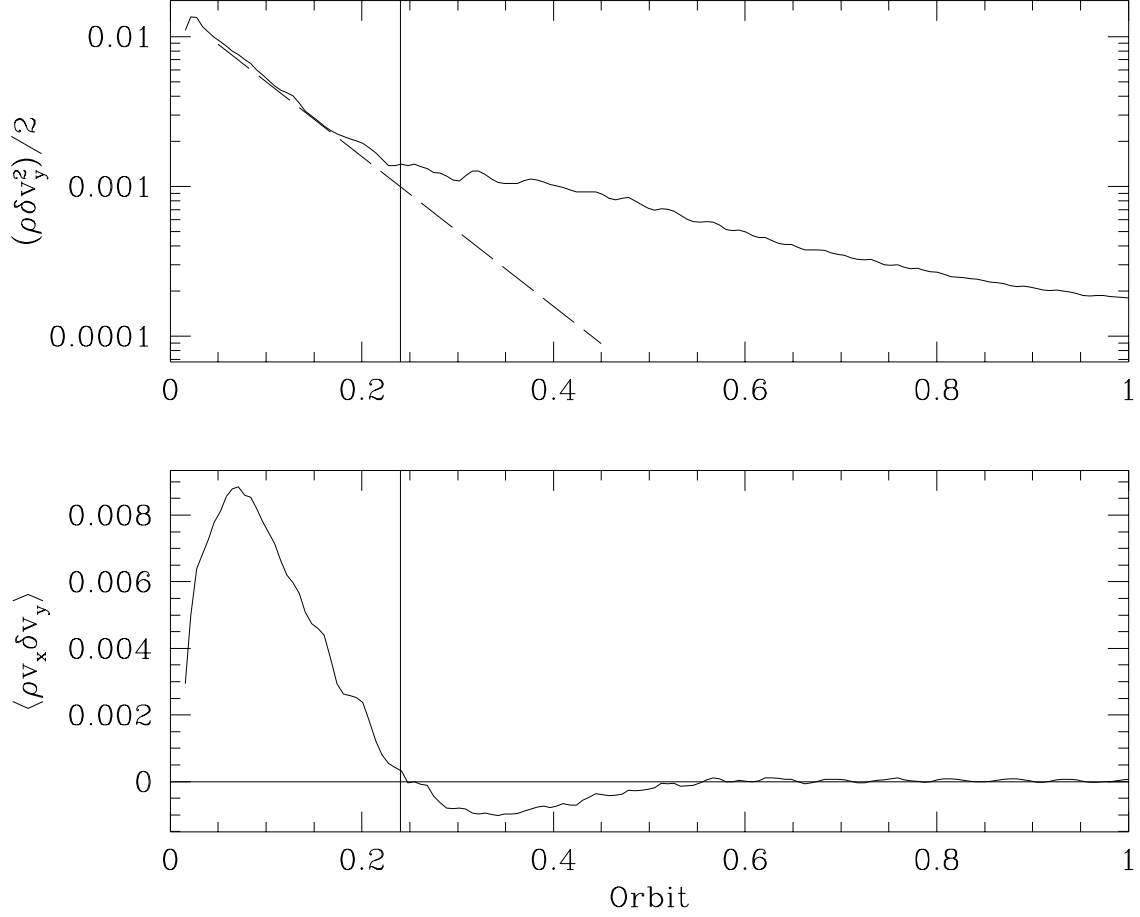


Fig. 3.— Time evolution of perturbed angular velocity kinetic energy and volume-averaged Reynolds stress for the 32^3 simulation. The abrupt change of slope in $\rho \delta v_y^2/2$ (dashed line added for reference) that occurs at $t = 0.24$ (indicated by vertical line) corresponds to the point in time when the Reynolds stress becomes negative. A negative Reynolds stress provides a source for angular velocity fluctuation energy; a positive Reynolds stress is a sink.

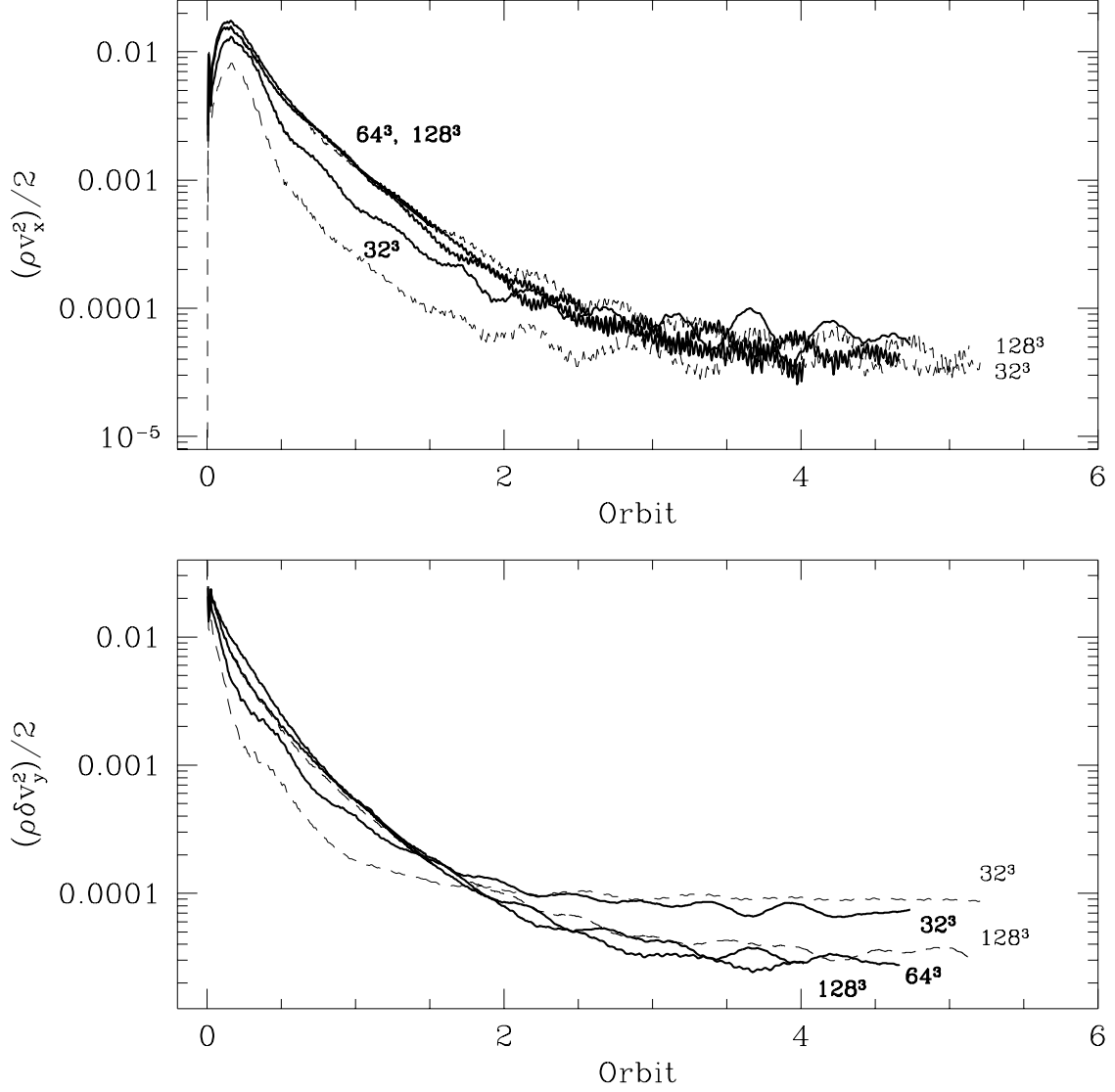


Fig. 4.— Evolution of v_x (top) and v_y (bottom) fluctuation kinetic energy for 3 simulations using the PPM algorithm with 32^2 , 64^3 , and 128^3 grid zones (bold curves). The 32^3 and 128^3 grid zone simulations from Figure 2 (dashed curves) are included for reference.

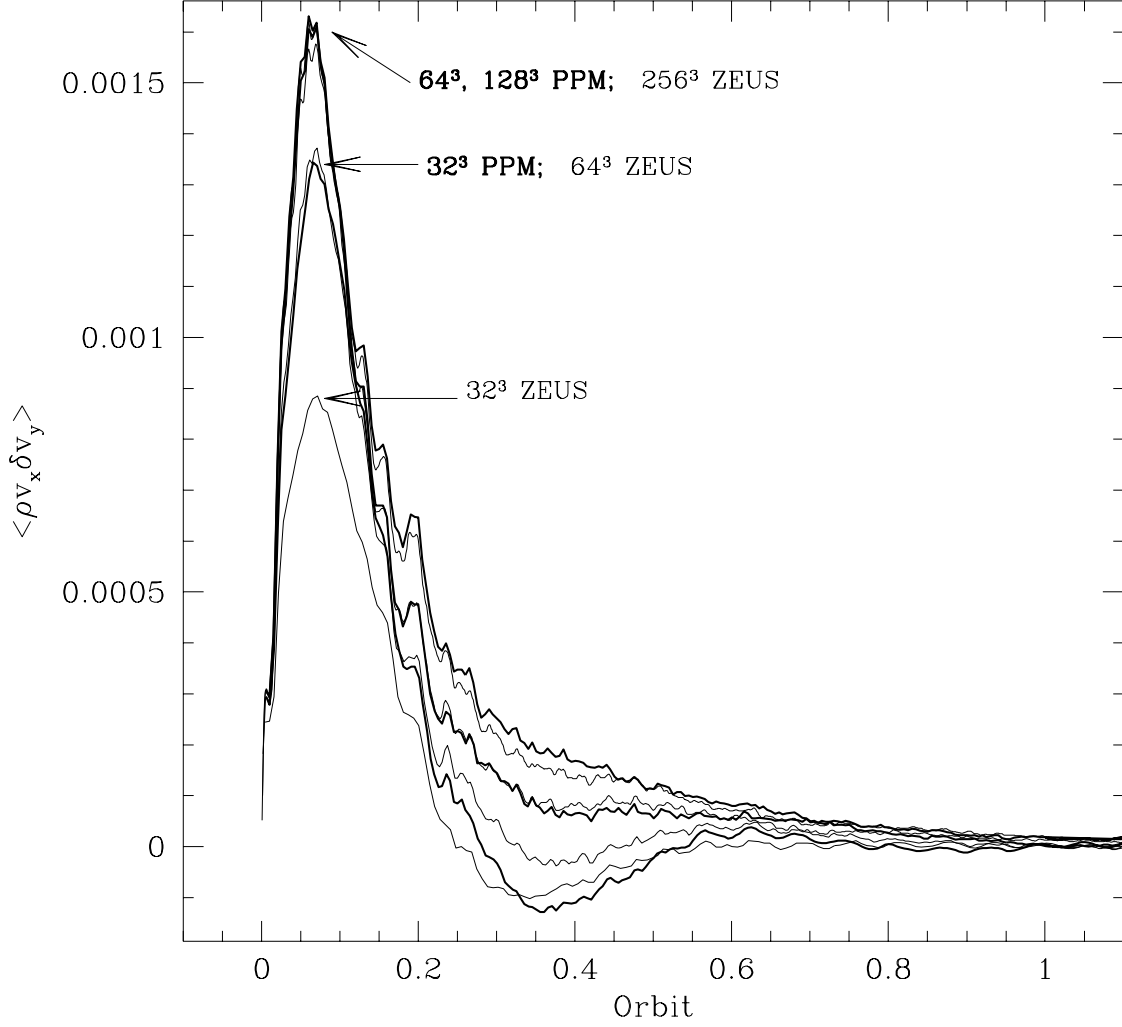


Fig. 5.— Time evolution of the Reynolds stress over the first orbit in the Keplerian simulations for a range of resolutions and for both the ZEUS and PPM (bold lines) numerical algorithms. The peak in the stress is labeled by the corresponding resolution and algorithm.

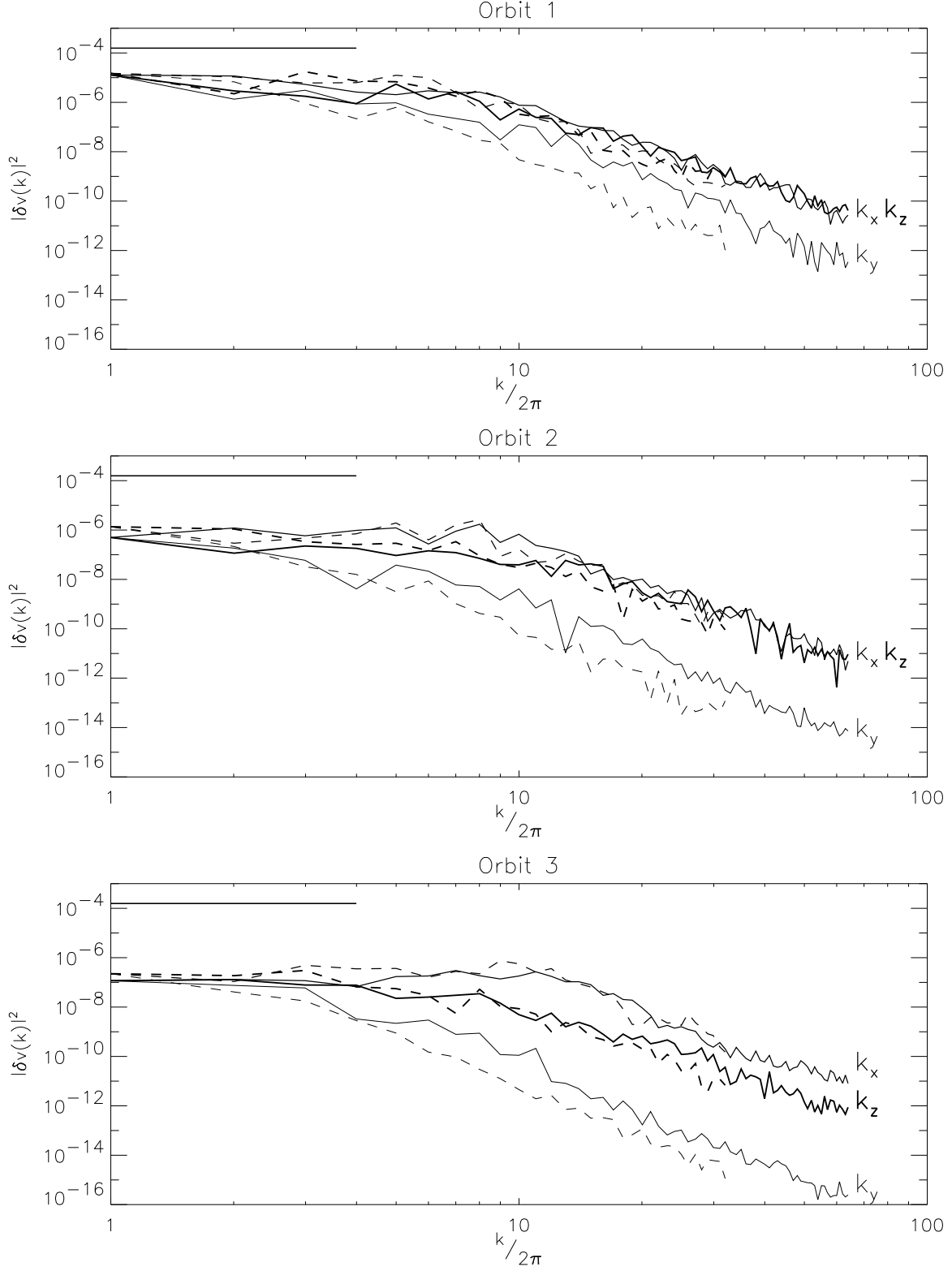


Fig. 6.— One dimensional power spectrum $|\delta v(k)|^2$ for the 128^3 (solid line) and 64^3 (dashed line) PPM Keplerian simulation at 1, 2 and 3 orbits. The horizontal line extending out to $k/2\pi = 4$ is power spectrum of the initial perturbation.

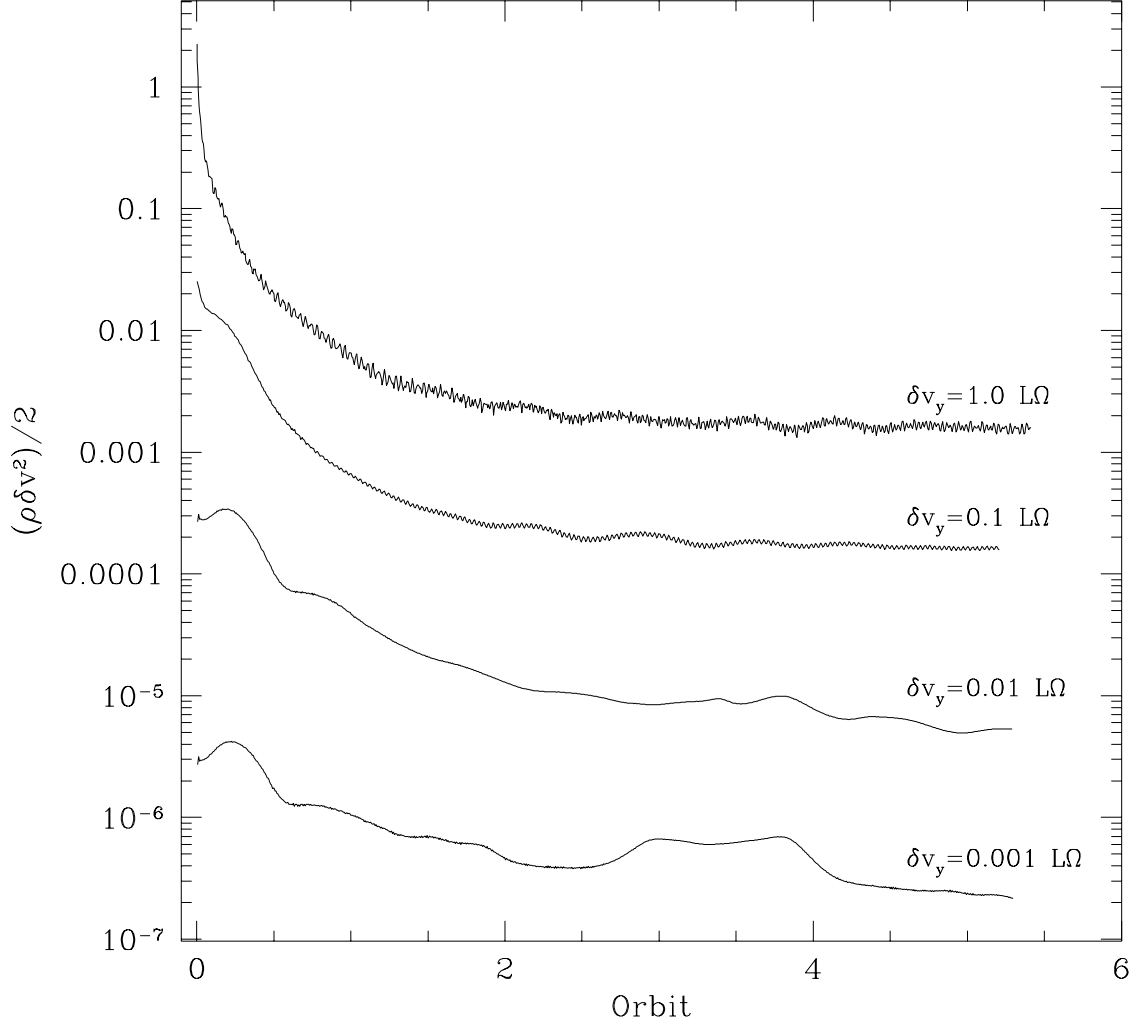


Fig. 7.— Time evolution of the perturbation kinetic energy in four 32^3 grid zone simulations of Keplerian shearing systems. The curves are labeled by the maximum amplitude of the initial perturbations. Larger initial perturbations show a larger rate of decay of the perturbed kinetic energy.

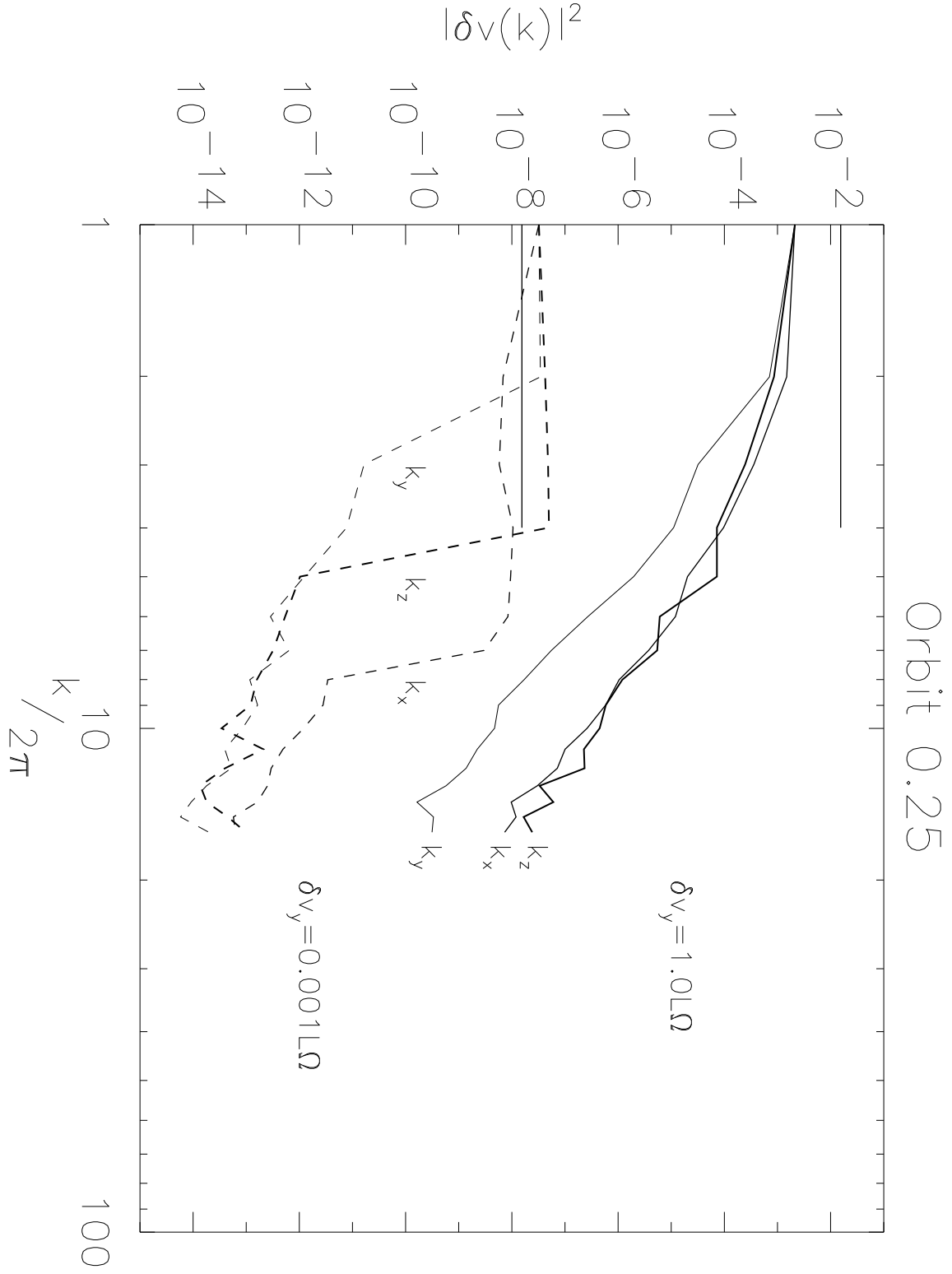


Fig. 8.— One dimensional power spectrum $|\delta v(k)|^2$ at 0.25 orbits for a 32^3 large amplitude perturbation simulation (solid line) and a 32^3 small amplitude perturbation simulation (dashed line). The curves are labeled by their initial maximum perturbation amplitude.

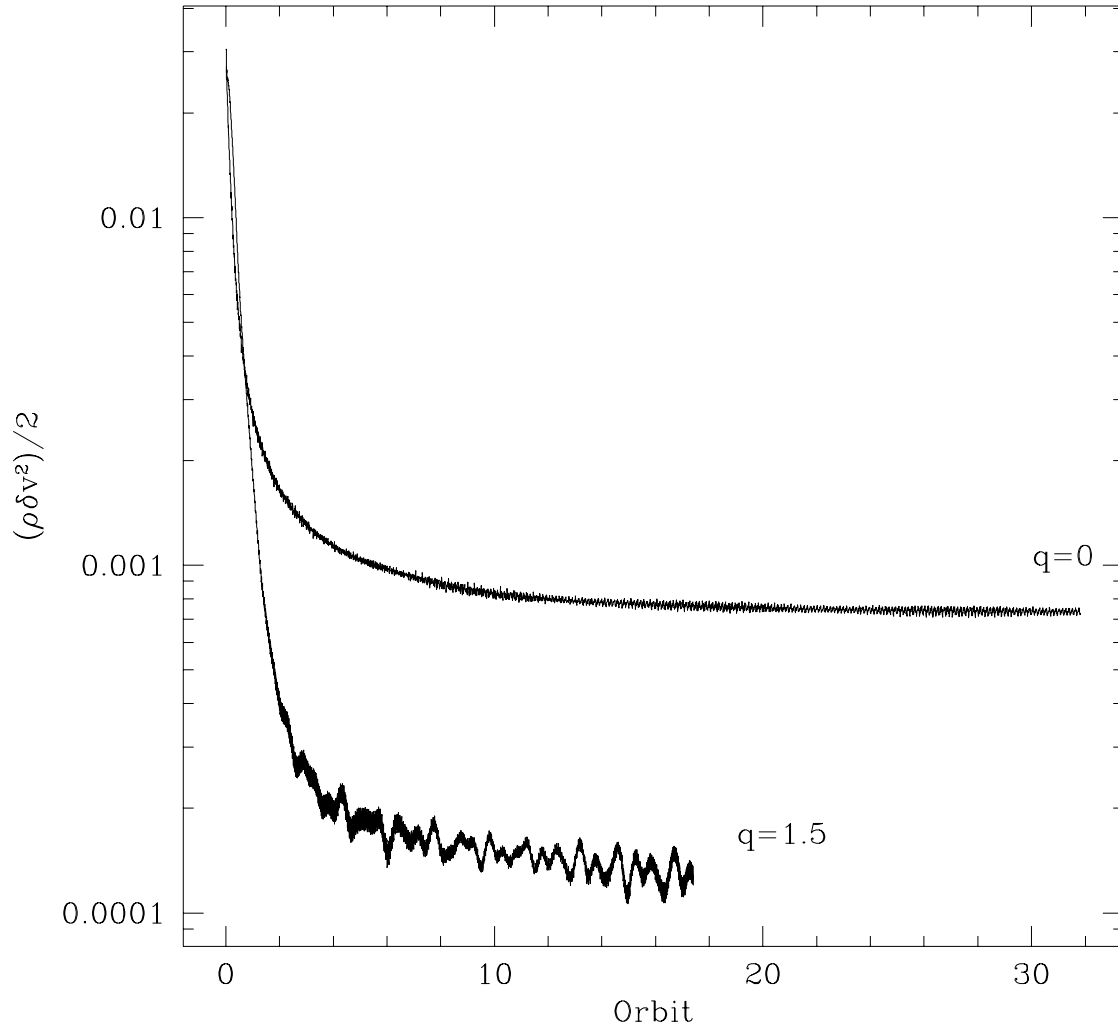


Fig. 9.— Time evolution of the perturbed kinetic energy in a constant Ω simulation, labeled $q = 0$, and a Keplerian simulation, labeled $q = 1.5$.

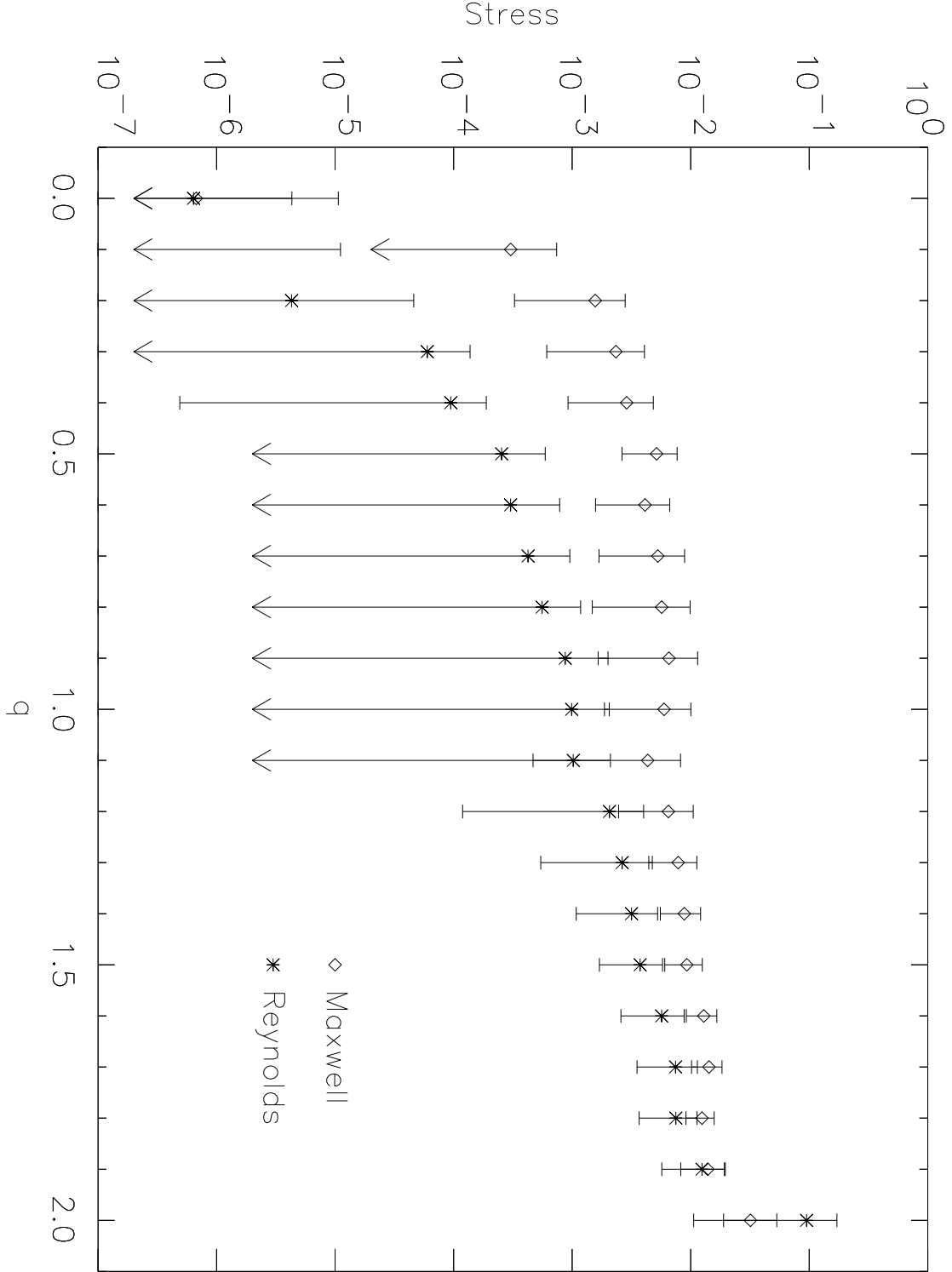


Fig. 10.— Reynolds stress (stars) and Maxwell stress (diamonds) for a series of MHD shearing box simulations with different background angular velocity distributions q . Stress values are time-averaged over the entire simulation. Error bars correspond to one standard deviation in the stress values.